IOPscience iopscience.iop.org

Home Search Collections Journals About Contact us My IOPscience

Strain contrast of GaN_yAs_{1-y} (y = 0.029 and 0.045) epitaxial layers on (100) GaAs substrates in annular dark field images

This article has been downloaded from IOPscience. Please scroll down to see the full text article.

2008 J. Phys.: Condens. Matter 20 075215

(http://iopscience.iop.org/0953-8984/20/7/075215)

View the table of contents for this issue, or go to the journal homepage for more

Download details:
IP Address: 129.252.86.83
The article was downloaded on 29/05/2010 at 10:34

Please note that terms and conditions apply.

J. Phys.: Condens. Matter **20** (2008) 075215 (7pp) doi:10.1088/0953-8984/20/7/075215

Strain contrast of GaN_yAs_{1-y} ($y = 0.029$ and 0.045) epitaxial layers on (100) GaAs substrates in annular dark field images

X Wu[1], M D Robertson[2], J A Gupta[1] and J-M Baribeau[1]

[1] Institute for Microstructural Sciences, National Research Council of Canada, Ottawa, ON, K1A 0R6, Canada
[2] Department of Physics, Acadia University, Wolfville, NS, B4P 2R6, Canada

E-mail: xiaohua@wu@nrc.ca

Received 13 September 2007, in final form 14 December 2007
Published 28 January 2008
Online at stacks.iop.org/JPhysCM/20/075215

Abstract
The annular dark field (ADF) image contrast of GaN_yAs_{1-y} ($y = 0.029$ and 0.045) epitaxial layers on (100) GaAs substrates was studied with a scanning transmission electron microscope (STEM) as a function of ADF detector inner semi-angles ranging from 28 to 90 mrad. Contradictory to the compositional contrast prediction of ADF-STEM image intensity, the lower average atomic number strained GaN_yAs_{1-y} layers were found to be brighter than the higher average atomic number GaAs for an ADF detector semi-angle up to 65 mrad. Multislice simulations reveal that the displacement around substitutional N atoms plays a crucial role in the observed ADF-STEM contrast, while the contribution to the contrast due to misfit strain between GaN_yAs_{1-y} and GaAs is small.

1. Introduction

The growth of semiconductor lattice-mismatched heteroepitaxial strained layers is technologically important for the development of modern opto-electronic devices. The use of strained layer structures provides new materials combinations whose electronic and opto-electronic properties are significantly modified through strain-induced changes in the electronic band structure [1]. Recently, there has been considerable interest in using so-called 'dilute nitrides', including GaN_yAs_{1-y}, $Ga_{1-x}In_xN_yAs_{1-y}$, and $Ga_{1-x}In_xN_yAs_{1-y-z}Sb_z$ as the active materials in semiconductor lasers grown on GaAs substrates. The incorporation of small amounts of nitrogen (N) into GaAs leads to a large decrease in the bandgap energy and has enabled the growth of GaAs-based laser diodes functioning in the 1.3–1.55 μm wavelength range [2–4].

An annular dark field scanning transmission electron microscopy (ADF-STEM) image is formed by scanning an electron beam across the surface of a sample and collecting the scattered electrons using an annular-shaped detector located in the diffraction plane of the microscope. High-angle ADF (HAADF) or Z-contrast imaging, in which the image contrast is sensitive to the variation in chemical composition, i.e. the atomic number Z, has been applied to the study of interfacial ordering in ultrathin SiGe superlattices [5], quantitative evaluation of SiO_2/Si interfaces [6] and a layer of Si buried in a GaAs matrix [7]. Z-contrast imaging has also been successfully applied to the observation of individual Sb dopant atoms in a low-Z crystalline Si matrix [8].

The contrast of an ADF-STEM image has also been shown to be dependent on strain, due to point defects and dislocations, for example. A study of B-doped layers in Si revealed significantly stronger contrast having opposite sign relative to simple atomic number contrast (Z-contrast) predictions [9]. It was suggested that misfitting substitutional B atoms act as point defect sites in a Si matrix which enhance scattering to high angles via a static Debye–Waller effect [9]. Furthermore, the effects of strain on the ADF-STEM image intensity at the interfaces of c-Si/a-SiO_2 (c = cubic, a = amorphous) [10] and c-Si/a-Si have been reported [11]. It was found that a bright band of contrast at the interface between c-Si/a-SiO_2 observed in ADF-STEM images could be attributed to a strain effect.

 © 2008 IOP Publishing Ltd Printed in the UK

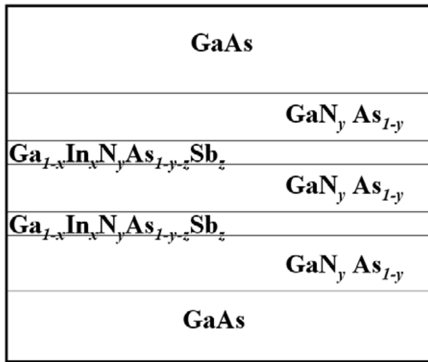

Figure 1. Schematic diagram of the double-quantum-well active region of a long-wavelength laser (1.55 μm range).

In the c-Si/a-Si interface, the sign of the strain contrast was observed to be dependent on specimen thickness as well as ADF detector angle.

In this study, defect-free tensile-strained GaN_yAs_{1-y} (y = 0.029 and 0.045) epitaxial layers grown on (100) GaAs substrates by molecular beam epitaxy (MBE) were studied in a STEM and a series of ADF images were obtained with detector inner semi-angles ranging from 28 to 90 mrad. Numerical simulations using a multislice formalism were performed in order to interpret the observed ADF-STEM image contrast of the strained GaN_yAs_{1-y} layers relative to the GaAs substrate.

2. Experimental details

Two samples of double-quantum-well (DQW) laser diode structures grown on (100) GaAs substrates by MBE were used for this study. Each active region contained two 7 nm thick $Ga_{1-x}In_xN_yAs_{1-y-z}Sb_z$ quantum wells and three 20 nm thick GaN_yAs_{1-y} barrier layers within a GaAs waveguide. The samples differ only in the N composition in the active region, with values of $Ga_{0.6}In_{0.4}N_{0.027}As_{0.961}Sb_{0.012}/GaN_{0.045}As_{0.955}$ and $Ga_{0.6}In_{0.4}N_{0.029}As_{0.959}Sb_{0.012}/GaN_{0.029}As_{0.971}$. Hereafter, each sample will be referred to by the N composition in the barrier layers (y = 0.029 and 0.045). A schematic diagram of the DQW laser diode structure at the ⟨011⟩ orientation is shown in figure 1. The details of the MBE growth including the control and determination of the N concentration and optical properties of the DQW laser have been reported previously [3, 4, 12]. All five layers in each active region are fully strained and free of defects [12, 13]. ⟨011⟩ cross-sectional TEM samples were prepared following standard dimpling and ion milling procedures. A 200 kV JEOL JEM-2100F TEM/STEM equipped with an ultra-high resolution pole piece (C_s = 0.5 mm), a Gatan ADF detector (5–11 mm active diameter), a Gatan DigiScan and a Gatan Imaging Filter (GIF) Tridiem was used for this study. An important parameter required in performing the image simulations was the electron probe size. The STEM probe used for this study was produced using the 'Free Lens Control' function in the JEM-2100F. Images of the probe and an intensity line profile across the centre of the probe are shown in figure 2. The probe displays a Gaussian profile and the full-width at half-maximum was 0.26 nm (figure 2(b)). Note that the probe size used in this study was larger than the minimum probe capabilities of the STEM (∼0.15 nm), but provided the beam current necessary for ADF-STEM imaging at the highest detector inner semi-angles. The probe convergence semi-angle was 14.3 mrad with a 40 μm diameter condenser lens aperture. Using the 'Free Lens Control' function in the JEM-2100F, a series of ADF detector inner semi-angles ranging from 28 to 90 mrad was created. The ADF detector inner semi-angles were calibrated by recording ⟨011⟩ zone axis GaAs diffraction patterns and the shadow image of the inner edge of the ADF detector simultaneously in the GIF CCD camera [14]. The ADF detector inner semi-angles used were 28, 37, 41, 50, 65, 76 and 90 mrad and the outer detector semi-angles were 2.2 times greater than the detector inner semi-angles. The Gatan ADF detector system includes 'gain' and 'brightness' adjustments in its control box. The brightness knob sets the background intensity and the gain knob scales the image by a multiplicative factor. Care has been taken to have these controls adjusted correctly in order to obtain accurate measurements [14].

3. Observations

Figure 3 displays seven ⟨011⟩ zone axis ADF-STEM images formed at ADF detector inner–outer semi-angles of 28–62 mrad, 37–81 mrad, 41–90 mrad, 50–110 mrad,

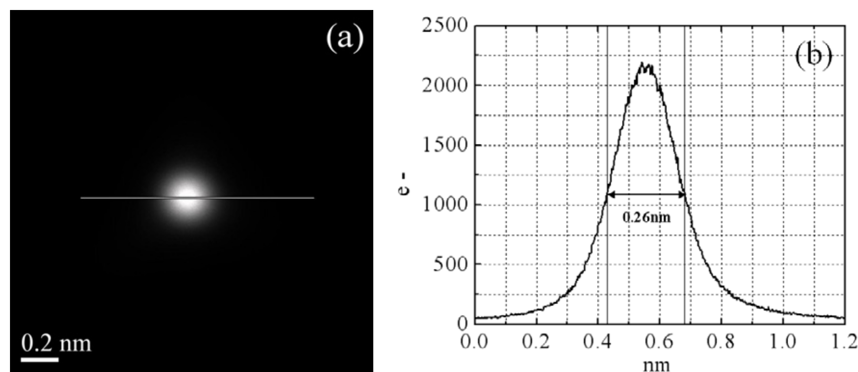

Figure 2. STEM probe size measurement: (a) measured probe intensity and (b) a line scan across the centre of the probe highlighting the FWHM of 0.26 nm.

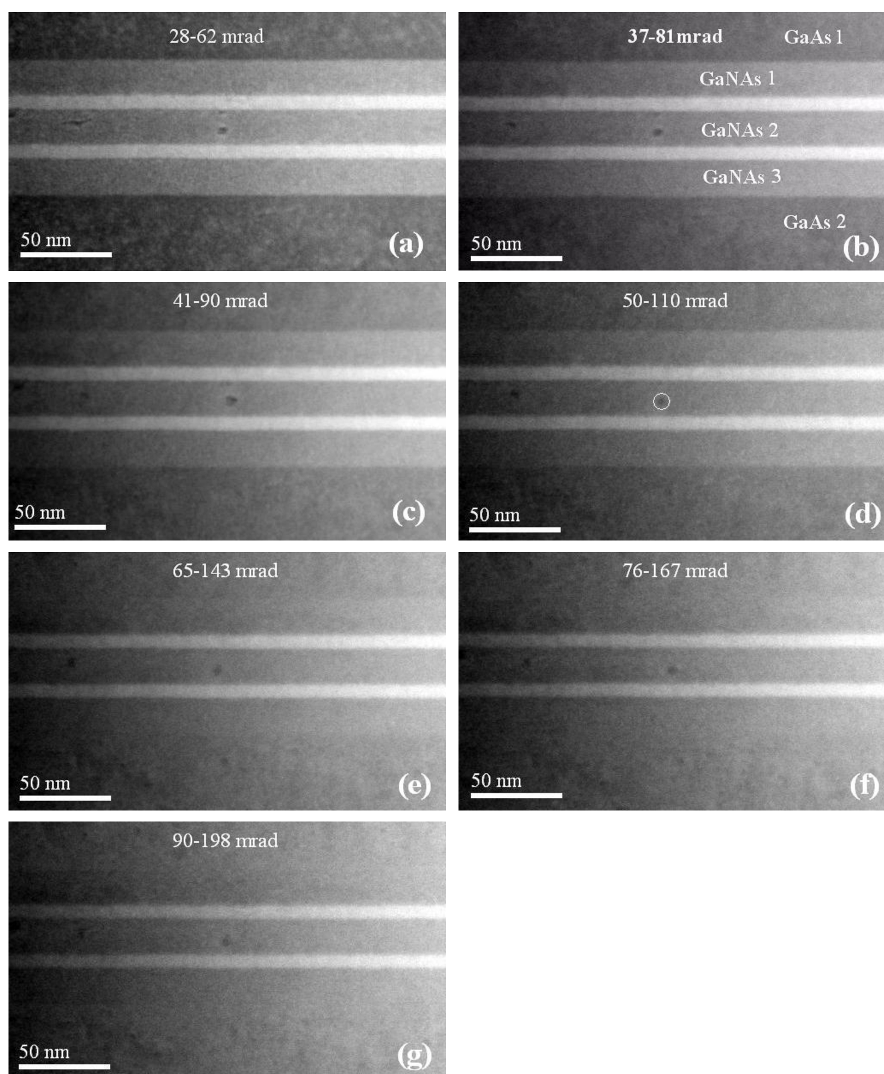

Figure 3. ADF-STEM images acquired at seven different detector angles for the $GaN_{0.045}As_{0.955}$ sample.

65–143 mrad, 76–167 mrad and 90–198 mrad for the $GaN_{0.045}As_{0.955}$ sample. The white circle in the middle of figure 3(d) highlights a marker used to ensure that all of the images were recorded at the same location, and the thickness of the specimen at the centre of the white circle is about 37 nm as determined from the ratio of the plasmon to the zero-loss peaks in electron energy-loss spectrum. It is observed that there is a large intensity difference between the $GaN_{0.045}As_{0.955}$ and GaAs layers at lower detector inner semi-angles, which decreases as the inner semi-angle increases. Contradictory to the compositional contrast prediction of ADF-STEM image intensity, the lower average atomic number $GaN_{0.045}As_{0.955}$ layers were brighter than the surrounding higher average atomic number GaAs for the ADF detector inner semi-angles up to 65 mrad (figures 3(a)–(e)). At the highest inner detector angle of 90 mrad (figure 3(g)), it is observed that the intensity of $GaN_{0.045}As_{0.955}$ is lower than that of GaAs. The overall increase in intensity from left to right in all of the images is due to increasing specimen thickness along this direction.

The $GaN_{0.029}As_{0.971}$ sample displays a similar relationship between the contrast and ADF detector angles, and two representative $\langle 011 \rangle$ zone axis ADF-STEM images acquired at ADF detector inner–outer semi-angles of 50–110 and 90–198 mrad are shown in figure 4. The most notable feature in figure 4 is that the intensity of $GaN_{0.029}As_{0.971}$ is higher than that of GaAs in the 50–110 mrad image (figure 4(a)), while the intensity of GaAs is higher in the 90–198 mrad image (figure 4(b)). The thickness of this specimen at the centre of the image is about 41 nm as determined from the low loss electron energy-loss spectrum.

Figure 5 displays intensity line profiles of the images shown in figures 3(d) and 4(a). The intensity line profiles were along the [100] direction, i.e. vertically across the layers and integrated over a width of 10 nm. The line scans clearly demonstrate that the GaN_yAs_{1-y} intensities are higher than that of GaAs for the images acquired at 50 mrad ADF detector inner semi-angle, but the contrast between GaN_yAs_{1-y} and GaAs is higher for the $GaN_{0.045}As_{0.955}$ sample (figure 5(a)) than for the $GaN_{0.029}As_{0.971}$ sample (figure 5(b)).

In order to quantitatively compare the intensity difference between the GaN_yAs_{1-y} and GaAs layers, the contrast (C) was

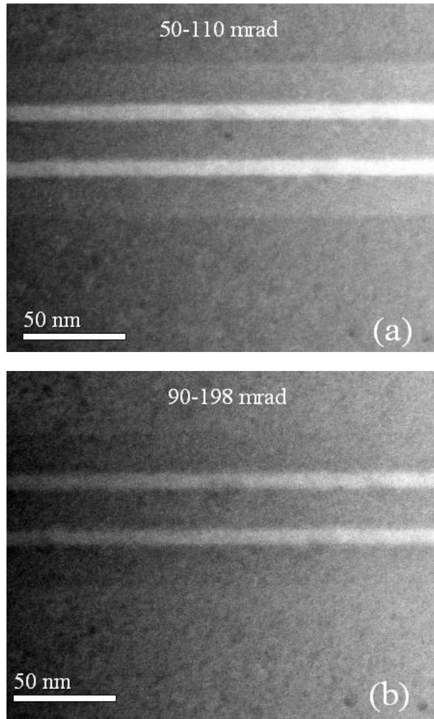

Figure 4. ADF-STEM images acquired at two different detector angles for the $GaN_{0.029}As_{0.971}$ sample.

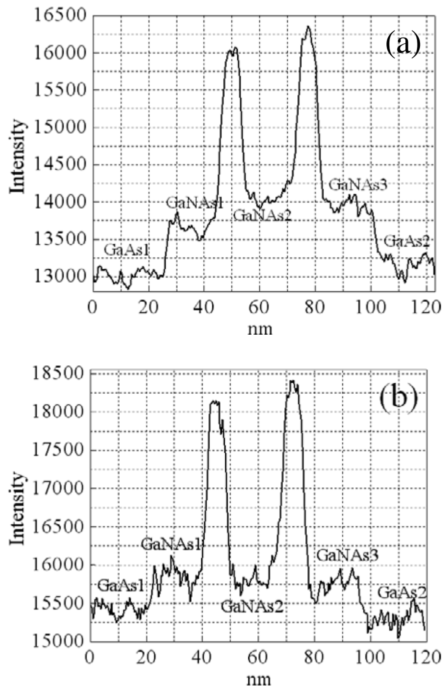

Figure 5. Intensity line profiles along the [100] direction from the images displayed in figures 3(d), (a) and 4(a), (b).

calculated from the expression

$$C = \left(I_{GaN_yAs_{1-y}}/I_{GaAs}\right) - 1 \quad (1)$$

where $I_{GaN_yAs_{1-y}}$ and I_{GaAs} are the intensities of GaN_yAs_{1-y} and GaAs layers, respectively. The intensity data for the GaAs matrix were obtained from the average of two 10 nm × 10 nm regions adjacent to the DWQ structure, and for the GaN_yAs_{1-y} layers the intensity from 10 nm × 10 nm regions from each of the three layers was averaged. The contrast measurement results are presented in figure 6 and the error bars are based on one-standard-deviation uncertainties. At a detector inner semi-angle of 28 mrad, the GaN_yAs_{1-y} intensity is higher than that of the GaAs layer and dependent on N concentration. The $GaN_{0.045}As_{0.955}$ and $GaN_{0.029}As_{0.971}$ intensities were about 13 and 9% higher than that of GaAs, respectively.

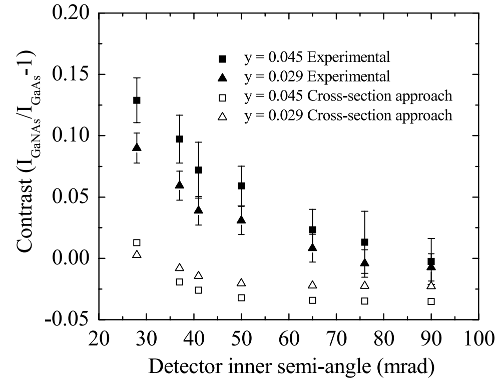

Figure 6. The experimental data of ADF-STEM image contrast between GaN_yAs_{1-y} and GaAs compared to the results from calculations using the atomic scattering cross-section approach.

4. Discussion

The higher ADF-STEM image intensity of the strained lower average atomic number GaN_yAs_{1-y} epitaxial layers than the neighbouring strain-free higher average atomic number GaAs layers for ADF detector inner semi-angles up to 65–76 mrad warrants further scrutiny. It is often assumed that for inner detector semi-angles greater than three times the probe convergence angle the image can be considered to be a HAADF image, where the image contrast is dominated by compositional effects. However, in the following discussion it will be shown that both compositional and strain contributions to the ADF-STEM image are required in order to explain the observed contrast between the GaN_yAs_{1-y} and GaAs layers.

For heteroepitaxial growth of GaN_yAs_{1-y} layers on a GaAs substrate, there is a misfit strain due to the difference in lattice constants of the two materials. Since the GaAs substrates are much thicker than the DQW layers, all of the strain can be assumed to be confined in the DQW layers and there is no strain in the GaAs substrates. The lattice constants of GaAs and GaN_yAs_{1-y} are 0.565 33 nm and 0.565 33–0.114 99y nm respectively [13]. The whole GaN_yAs_{1-y} film is under biaxial tensile strain and the strain is accommodated by the tetragonal distortion of the GaN_yAs_{1-y} lattice [13]. Considering a coordinate system in which the y axis is parallel to the (100) growth direction and the plane containing the x and z axes is parallel to the film–substrate interface plane, after the epitaxial growth, the lattice constants of GaAs remain at the bulk values of $a = b = c =$

0.565 33 nm. For the tensile-strained GaN_yAs_{1-y} films, the in-plane lattice parameters are constrained to match the substrate values, $a = c = 0.565\,33$ nm, so the strain displacement along x and z directions is 0.005 17 nm for $GaN_{0.045}As_{0.955}$, and 0.003 34 nm for $GaN_{0.029}As_{0.971}$ respectively. From linear elasticity theory, the perpendicular lattice constant of the film, b, is given by $(1 - \frac{2\nu}{1-\nu} f)a$ and has the smaller value $b = 0.555\,43$ nm for the $GaN_{0.045}As_{0.955}$ film and $b = 0.558\,96$ nm for the $GaN_{0.029}As_{0.971}$ film. Lattice misfit strain gives the average effects of strain over a large volume; however, on an atomic scale there are significant local variations in the strain arising from radial displacements around substitutional N atoms in the GaN_yAs_{1-y} lattice because the N atomic radius of 0.068 nm is much smaller than the 0.121 nm atomic radius of the As host atoms. It will be shown that these local variations in the strain can lead to significant high-angle scattering and greater image contrast than would be expected from scattering cross-section or uniform strain considerations alone.

4.1. Atomic scattering cross-section considerations

The simplest way to model the effect of strain fields on observed image contrast is to consider the changes in the atomic scattering cross-section arising due to strain. For defect-free crystals at a zone axis orientation, the intensity of the ADF-STEM image can be approximated by a thermal diffuse scattering model (TDS) [10, 11], and the differential cross-section for the TDS is given by [15, 16]

$$\left[\frac{d\sigma(\theta)}{d\Omega}\right]_{\mathrm{TDS}} = \frac{4\gamma^2 Z^2}{a_0^2 k_0^4} \frac{1}{(\theta^2+\theta_0^2)^2} \left[1-\exp(-2\left(M^T\right)\theta^2)\right] \tag{2}$$

where $\theta_0 = (k_0 r_0)^{-1}$ is the characteristic angle of elastic scattering, $k_0 = 2505\ \mathrm{nm}^{-1}$ is the wavevector (at 200 keV), $r_0 = a_0 Z^{-1/3}$ is the screening radius, $a_0 = 0.0529$ nm is the first Bohr radius, $\gamma = 1.394$ (at 200 keV) is the relativistic factor and Z is the average atomic number. $M^T = 8\pi^2 u_T^2/\lambda^2$ is the Debye–Waller factor and u_T is the amplitude of the thermal vibrations. At room temperature, $u_T = 0.09$ Å for Ga and As [17]. The scattering of the incident electrons from a random strain field can be treated similarly to that from TDS [10, 11] and an extra Debye–Waller factor can be added to the cross-section of TDS scattering to account for the strain effect:

$$\left[\frac{d\sigma(\theta)}{d\Omega}\right]_{\mathrm{TDS+Strain}} = \frac{4\gamma^2 Z^2}{a_0^2 k_0^4} \frac{1}{(\theta^2+\theta_0^2)^2} \times \left[1-\exp\left(-2\left(M^T+M^S\right)\theta^2\right)\right] \tag{3}$$

where $M^S = 8\pi^2 u_S^2/\lambda^2$ and u_S is the amplitude of the strain. In this study, the values of u_S used are 0.005 17 nm and 0.003 24 nm for $GaN_{0.045}As_{0.955}$ and $GaN_{0.029}As_{0.971}$, respectively.

The intensity collected by the ADF detector can be calculated by integrating the cross-section over the detector geometry and it is shown in figure 4. Although the random strain increases the ADF-STEM image intensity for lower detector inner semi-angles, the overall contrast does not agree with the measured contrast to within experimental uncertainty. The maximum calculated contrast using the cross-section model was only 1.3% for $GaN_{0.045}As_{0.955}$ and 0.3% for $GaN_{0.029}As_{0.971}$ at a detector semi-angle of 28 mrad. For ADF detector inner semi-angles larger than 50 mrad, the cross-section model predictions converge to follow the simple rule that the ADF-STEM image intensity depends on Z^2, i.e. $(31.415/32)^2 - 1 = -0.0362$ and $(31.623/32)^2 - 1 = -0.0234$ for $y = 0.045$ and 0.029, respectively.

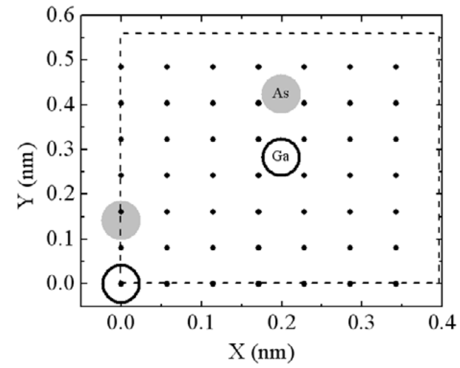

Figure 7. The unit cell for ⟨011⟩ GaAs, indicating the locations of the Ga atoms (open circles), As atoms (grey circles) and the 7 × 7 array (small solid circles) of sampling points where the intensity was individually calculated and then averaged to obtain the final image intensity.

4.2. Multislice calculations

The discrepancy between the experimental contrast measurements and predictions based on an atomic scattering cross-section model is not surprising considering that the scattering cross-section approach neglects some important experimental factors that contribute to the ADF-STEM image intensity such as sample thickness, beam convergence angle, probe size, multiple electron scattering effects and a non-random strain field. A more realistic model where these factors have been incorporated is required to interpret the observed contrast in the ADF-STEM images, and multislice calculations employing a GaAs-based supercell were used to accurately simulate the ADF-STEM image intensity.

The primitive unit cell for GaAs in the ⟨011⟩ zone axis orientation is displayed in figure 7 and the repeat distances in the x, y and z directions are 0.3997 nm, 0.5653 nm and 0.3997 nm, respectively. This choice of unit cell is not square and was repeated four times in the x direction and three times in the y direction, creating a supercell that is nearly square and suitable for fast Fourier transform processing in the multislice calculations. The unit cell in the z direction is repeated to achieve a total specimen thickness of 41 nm. In the multislice calculations, the sample is sorted into a series of thin layers as a function of specimen thickness where each layer is set to 0.3997 nm thick, and the electron beam is propagated sequentially through each layer. The ADF-STEM image intensity is obtained by integrating the intensity of the convergent beam electron diffraction pattern over the range of inner and outer semi-angles of the detector for each pixel in the image.

The simulation parameters used in the multislice calculations are a spherical aberration coefficient (C_s) of 0.5 mm, an electron beam energy of 200 keV, a wavefunction size of 512 × 512 pixels and a beam convergence angle of 6.0 mrad. This convergence angle was intentionally set smaller than the experimental value of 14.3 mrad in order to simulate a near Gaussian shaped probe with the same FWHM of 0.26 nm as recorded experimentally (figure 2(b)). The condenser lenses were set to obtain a higher beam current to reduce noise in the image rather than to obtain the minimum probe size as expected in an ideal simulation. The defocus used was 26.6 nm as given by the 'most compact probe' criteria [18].

Since the images presented in figures 3 and 4 do not display the crystalline lattice, the average measured intensity is a result of the probe scanning a variety of positions within the unit cell. That is, some of the pixels were located over atomic columns and others between the columns at various distances. In order to simulate this averaged intensity, the simulated intensities were calculated in a 7 × 7 array within the unit cell at locations indicated by the small dots in figure 7. Specifically, a full multislice calculation was performed, where the electron probe was located at each of the 7 × 7 locations and the intensity calculated. The intensities were then summed incoherently over these 49 positions to achieve the image intensity. This procedure was repeated 32 times for 32 different atom configurations to accurately simulate the effects of thermal diffuse scattering as a result of lattice vibrations in the frozen phonon approximation [19].

The code of Kirkland [19] was used to perform the multislice simulation calculations and was modified to allow for more automated operation. Loops were added to program 'autoslic' [19] so that the electron beam intensity could be calculated at each of the 49 sampling points as well as for a given number of thermal vibration configurations, in this case 32. These changes required the electron probe calculation (program 'probe' [19]) to be added as a function in program 'autoslic'. Furthermore, the transmission functions for each of the multislice layers were calculated once and stored in memory so that they could be reused for each of the 49 sampling points. The transmission functions were recalculated for each frozen phonon configuration since the location of the atoms in the supercell will have shifted slightly for each configuration. Although this significantly increased the amount of memory required for the program to run, the computational time decreased by a factor of about four.

Two different models of the strain in the GaN_yAs_{1-y} layer were used for the multislice calculations: (1) uniform misfit strain and (2) local strain around the substitutional N atoms. Over the dimensions of the supercell both models incorporated the same average lattice misfit, but in the substitutional N-atom model there are localized regions of relatively large atomic shifts that lead to enhanced high-angle scattering of the imaging electrons.

As discussed at the beginning of section 4, the misfit strain in the GaN_yAs_{1-y} film is accommodated by a tetragonal distortion of the GaN_yAs_{1-y} lattice. The lattice constants of the GaN_yAs_{1-y} films after the uniform tetragonal distortion are $a = c = 0.565\,33$ nm, $b = 0.555\,43$ nm for the

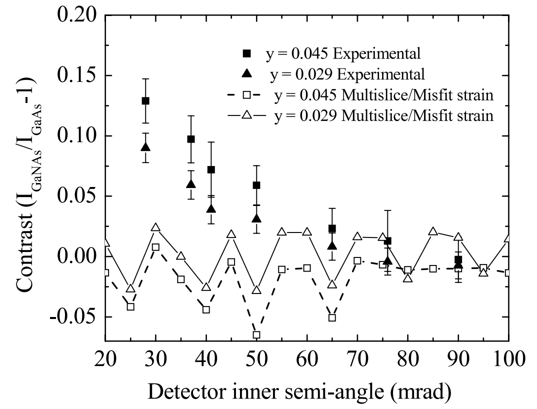

Figure 8. The experimental data of ADF-STEM image contrast between GaN_yAs_{1-y} and GaAs compared to the results from multislice calculations using the misfit strain model.

$GaN_{0.045}As_{0.955}$ film and $a = c = 0.565\,33$ nm, $b = 0.558\,96$ nm for the $GaN_{0.029}As_{0.971}$ film. Figure 8 is the multislice simulation results using the misfit strain model with the above lattice constants for the GaAs and GaN_yAs_{1-y} layers. A peculiar feature of figure 8 is that the contrast fluctuates significantly below the experimental data. The mild oscillatory nature of the calculated contrast is believed to be due to a shift in the angle of the Bragg diffracted spots with a change in the GaN_yAs_{1-y} lattice parameters with respect to GaAs. This shifting of the diffracted intensity will cause a subset of the Bragg reflections from the GaN_yAs_{1-y} to differ from those of GaAs for the same range of detector angles and depending on the exact reflections involved could lead to either brighter or darker contrast with detector angle. For both samples investigated there is poor agreement between theory and experiment for all but the two highest detector semi-angles and a more detailed model is required to explain the observed image contrast.

In the local strain model, the N atoms in the GaN_yAs_{1-y} layers were randomly substituted within a GaAs matrix, replacing each arsenic (As) atom with a probability equal to the y value of the GaN_yAs_{1-y} film. The displacement ($\mathbf{u}$) of the atoms surrounding each substitutional N atom due to the atomic radius difference of As and N atoms was modelled using linear elasticity theory in the isotropic approximation as

$$\mathbf{u} = (c/r^3)\mathbf{r}, \tag{4}$$

where c is a constant dependent on the degree of lattice distortion around the N atoms and r is a position vector in the lattice. An estimate of c was determined theoretically from elasticity theory [20],

$$\frac{\mathrm{d}a}{a} = 4\pi \frac{1-\nu}{1+\nu} \frac{nc}{\Omega}, \tag{5}$$

where $n = y/2$ is the N concentration, $\nu = 0.312$ is Poisson's ratio for GaAs, $\mathrm{d}a/a$ is a measure of the lattice misfit with $\mathrm{d}a = a_{\mathrm{GaAs}} - a_{\mathrm{GaN}_y\mathrm{As}_{1-y}} = 0.114\,99y$ nm and $\Omega = 22.55 \times 10^{-3}$ nm^3 is the atomic volume. Substituting these values into equation (5) gives $c = 1.4 \times 10^{-3}$ nm^3. The magnitude of the atomic displacements predicted using equations (4)

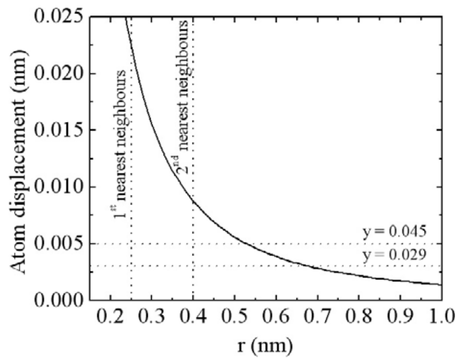

Figure 9. A plot of the atomic displacements (solid curve) due to the substitution of a N atom for an As atom in a GaAs matrix as estimated using equations (4) and (5). The intersections of the vertical dotted lines with the solid curve indicate the magnitudes of the atomic displacements at the locations of the first and second nearest neighbour atoms, whereas the intersections of the horizontal dashed lines with the solid curve give the magnitudes of the atomic displacements due to uniform lattice misfit strain.

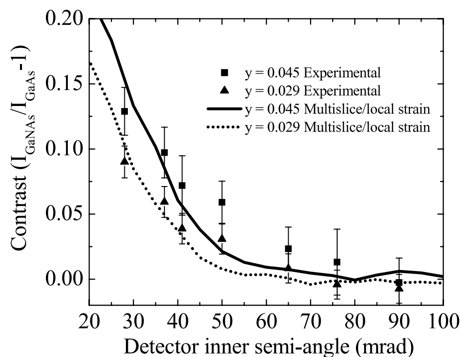

Figure 10. The experimental data of ADF-STEM image contrast between GaN_yAs_{1-y} and GaAs compared to the results from multislice calculations using the local strain model.

and (5) is plotted in figure 9 and it is observed that for the first and second nearest neighbour atoms the displacements are significantly greater than those arising from uniform lattice misfit strain. Furthermore, the atomic displacements in the substitutional model are not uniform, but are radial in nature, and the combined effects of N substitution for As in the GaAs matrix, non-uniform atomic displacements and larger magnitude of displacement were expected to lead to enhanced non-Bragg scattering of the electron intensity onto the ADF detector. The results from the multislice simulations are plotted in figure 10, and the model contrast agrees very well with the experimental contrast since most of the data are located within the one-standard-deviation uncertainly limits with respect to the model. Image contrast calculated from the N-substitutional model correctly reproduced the increasing contrast with lower detector inner semi-angle as well as the lower image contrast with reduced N concentration in the layers.

5. Conclusions

The experimental ADF-STEM image contrast between strained GaN_yAs_{1-y} layers and the GaAs substrate was observed to decrease with increasing ADF detector inner semi-angle and with decreasing N concentration. Contradictory to the compositional contrast prediction of ADF-STEM image intensity, the lower average atomic number GaN_yAs_{1-y} layers were brighter than the surrounding higher average atomic number GaAs for ADF detector semi-angles up to 65 mrad. For ~40 nm thick specimens and 28 mrad ADF detector inner semi-angle, the $GaN_{0.045}As_{0.955}$ and $GaN_{0.029}As_{0.971}$ intensities are about 13% and 9% higher than that of GaAs, respectively. For a 28 mrad detector semi-angle, the atomic scattering cross-section calculations show that a random strain field gives only ~1.3% contrast for $GaN_{0.045}As_{0.955}$ and ~0.3% contrast for $GaN_{0.029}As_{0.971}$, respectively. Multislice simulations reveal that the contribution to the contrast due to uniform misfit strain between the GaN_yAs_{1-y} film and GaAs is small, while displacement around substitutional N atoms plays a critical role in the observed ADF-STEM contrast. There is very good agreement between the observed contrast and multislice calculations using the N-substitutional local strain model.

Acknowledgments

T Aoki and M Kawasaki of JEOL USA are acknowledged for their assistance in the STEM probe size measurement.

References

[1] O'Reilly E P 1989 *Semicond. Sci. Technol.* **4** 121
[2] Wei S H and Zunger A 1996 *Phys. Rev. Lett.* **76** 664
[3] Gupta J A, Barrios P J, Pakulski G, Zhang X and Wu X 2005 *Electron. Lett.* **41** 1061
[4] Gupta J A, Barrios P J, Caballero J A, Poitras D, Aers G C, Pakulski G and Wu X 2006 *Appl. Phys. Lett.* **89** 151119
[5] Jesson D E, Pennycook S J and Baribeau J-M 1991 *Phys. Rev. Lett.* **66** 750
[6] Nakanishi N, KiKuchi Y, Yamazaki T, Okunishi E, Watanabe K and Hashimoto I 2004 *Phys. Rev.* B **70** 165324
[7] Carlino E and Grillo V 2005 *Phys. Rev.* B **71** 235303
[8] Voyles P M, Muller D A, Grazul J L, Citrin P H and Gossmann H-J 2002 *Nature* **416** 826
[9] Perovic D D, Rossouw C J and Howie A 1993 *Ultramicroscopy* **52** 353
[10] Duscher G, Pennycook S J, Browning N D, Rupangudi R, Takoudis C, Gao H J and Singh R 1998 *Characterization and Metrology for ULSI Technology* (New York: American Institute of Physics) p 191
[11] Yu Z, Muller D A and Silcox J 2004 *J. Appl. Phys.* **95** 3362
[12] Gupta J A, Sproule I S, Wu X and Wasilewski Z R 2006 *J. Cryst. Growth* **291** 86
[13] Wu X, Baribeau J-M, Gupta J A and Beaulieu M 2005 *J. Cryst. Growth* **282** 18
[14] Wu X, Robertson M D, Gupta J A, Baribeau J-M, Bennett J C, Kawasaki M and Aoki T 2007 *Mater. Res. Soc. Symp. Proc.* **982E** KK01-03
[15] Egerton R F 1996 *Electron Energy-loss Spectroscopy in the Electron Microscope* 2nd edn (New York: Plenum) p 134
[16] Hall R and Hirsch P B 1965 *Proc. R. Soc.* A **286** 158
[17] Reid J S 1983 *Acta Crystallogr.* A **39** 1
[18] Spence J C H 2003 *High Resolution Electron Microscopy* 3rd edn (New York: Oxford University Press) p 252
[19] Kirkland E J 1998 *Advanced Computing in Electron Microscopy* (New York: Plenum)
[20] Hall C R, Hirsch P B and Booker G R 1966 *Phil. Mag.* **14** 979